



OPEN Investigating the first case of permafrost degraded subsidence in Lahaul & Spiti region of Tethyan Himalayas

Kirti Kumar Mahanta, Ipshita Priyadarsini Pradhan, Nitesh Dhiman, Ankit Singh & Dericks Praise Shukla

Rising temperatures and changing precipitation patterns are causing rapid changes in the Himalayan ecosystem. Changes in climatic conditions affect various aspects of high mountain environments, including glaciers, rock glaciers, and permafrost, and pose significant threats to indigenous mountain communities. This study investigates the first case of permafrost thaw-induced subsidence in the Lindur Village of Lahaul & Spiti district of Himachal Pradesh using MT-InSAR method. We used 15 Sentinel-1 single-look complex images acquired from April 2022 to September 2022 along the ascending orbit track and used the SBAS technique to monitor the subsidence in the village. The results revealed significant land subsidence rates ranging from 7.9 to -6.8 cm/year. The cumulative land subsidence of 16 cm was observed over the northeast direction of the village. The analysis of historical temperature and precipitation data from 1950 to 2024 shows a significant rise in temperature at a rate of 0.02 °C/year and a shift in precipitation pattern over the village. From the field observations, the study found that the local geology and existing rock glaciers exacerbate the rate of subsidence leading to the development of cracks in the region. This is the first study that provides a detailed insight into the interaction of climatic, geological, and hydrological factors that drive permafrost thaw causing land subsidence in the Indian Tethyan Himalayas. The quantified deformation rates provide crucial information for developing targeted mitigation strategies and early warning systems.

Keywords Permafrost, MTInSAR, Land subsidence, Climate change, Time series analysis

Permafrost, an essential climatic variable of the cryosphere, is defined as a layer of soil or rock that remains at or below 0°C for at least two consecutive years^{1–3}. It covers approximately 25% of the Earth's land surface^{4,5}. Although the Arctic holds the majority of the area with continuous permafrost landscapes, mountain regions such as the Himalayas and the Qinghai-Tibet Plateau (QTP) also present significant permafrost^{6,7}. The Himalayan permafrost situated in areas such as Ladakh, Uttarakhand, and Himachal Pradesh is characterized by discontinuous and sporadic patches influenced by steep topography, elevation and microclimatic variations^{8–10}. These permafrost areas, which are less studied than their arctic counterparts, are crucial for sustaining regional water resources and maintaining ecosystem stability. Previous studies have confirmed the presence of permafrost in the Himalayas via a combination of field surveys and remote sensing techniques^{11–19}. The studies have considered active rock glaciers, ice-cored moraines, and talus slopes as geomorphological indicators of permafrost occurrence²⁰.

Permafrost is extremely sensitive to climate change and often considered as a key indicator of shifting climatic conditions^{21–24}. With rising temperatures and accelerated thawing, permafrost poses a severe threat to Himalayan communities and infrastructure^{25–27}. Recent projections indicate that the increase in permafrost degradation in the region could significantly influence local hydrological and geomorphic changes, such as increased rockfalls, landslides, and ground subsidence^{28–33}. Degradation also poses a serious threat to the ecological process; livelihoods of indigenous mountainous community and engineering structures present in the area. Unlike Arctic regions, the permafrost in the Himalayas is highly sensitive to climatic fluctuations due to the relatively low ground ice content and steep gradients, which further increase the region's vulnerability^{29,30,34–36}.

Recent advances in remote sensing technologies, particularly interferometric synthetic aperture radar (InSAR), InSAR have made InSAR of critical importance in monitoring permafrost degradation at global and

DExTER Lab, School of Civil and Environmental Engineering, Indian Institute of Technology Mandi, Mandi 175005, India. email: dericks@iitmandi.ac.in

regional scales^{37–39}. The detection of surface deformation associated with permafrost subsidence using InSAR techniques, such as differential interferometric synthetic aperture radar (D-InSAR), persistent scatter InSAR (PS-InSAR), and small baseline subset InSAR (SBAS-InSAR), differ in their capabilities in monitoring permafrost subsidence^{39–41}. D-InSAR uses pairs of radar images to measure ground displacement and is usually affected by temporal and spatial decorrelation in areas with dynamic surface changes or dense vegetation⁴². PS-InSAR addresses some of these limitations by analyzing coherent scatterers such as bridges, buildings or rocks over a time series of radar images⁴³. This technique enhances precision in urban areas or areas with less vegetation but is less effective in rugged terrain and snow mountains, such as those in the Himalayas^{44–46}. PS-InSAR is less effective in these areas due to the irregular and sparse distribution of persistent scatterers. Similarly, SBAS-InSAR focuses on minimizing temporal decorrelation by using small temporal and spatial baselines in interferogram generation, making it more suitable for deformation mapping⁴⁷. However, permafrost degradation is a slow-moving process and is difficult to monitor with pairs of radar images. MT-InSAR has emerged as a key tool for monitoring slow-moving processes such as permafrost subsidence^{48,49}. It integrates long time series of radar images to capture surface deformation more accurately than other methods do.

Recent studies have demonstrated the effectiveness of InSAR in identifying surface deformation in permafrost regions like the QTP and Alaska using data from Envisat, ALOS, TerraSAR-X, and Sentinel-1 satellites^{50–55}. Himalayan permafrost is not immune to degradation trends observed by QTP and Alaska. Despite this advancement, the application of MT-InSAR for permafrost degradation monitoring in the Himalayas remains rare. Although several studies have mapped the extent of permafrost over the Himalayas, studies related to permafrost-induced subsidence are relatively scarce. Therefore, to understand permafrost degradation across the Himalayan region, this study utilized MT-InSAR techniques to analyze the spatial and temporal advancement of permafrost degradation-induced subsidence over a Himalayan village. By analyzing climatic variables and local geology, this study aims to provide a comprehensive understanding of the degradation process affecting a village and its surrounding areas.

Study area

Lindur village is situated in the northwestern part of the Lahaul and Spiti districts of Himachal Pradesh (Fig. 1). The village covers an area of 43.09 hectares and is situated at an average elevation of 3328 m from the mean sea level. According to the 2011 census, the village comprises a small village/hamlet in Lahaul Tehsil in Lahaul and Spiti District of Himachal Pradesh, India, and it comes under Gohrma Panchayat. It is located 31 km northwest from District headquarters Keylong and 182 km from the state capital Shimla. In Lindur village, children aged 0–6 years account for 4.17% of the total population, with a total of 3 children in this age group. The village has an average sex ratio of 946, which is below the Himachal Pradesh state average of 972. However, the child sex ratio in Lindur is 2000, compared to the state average of 909. The literacy rate in Lindur village is lower than the state average, standing at 69.57% in 2011, while Himachal Pradesh had a literacy rate of 82.80%. In Lindur, male literacy is 77.78%, whereas female literacy is 60.61%. (Census 2011).

The region lies in the rain shadow of the GHR (Great Himalayan Range), resulting in low annual rainfall ranging in between 10 to 40 cm. This makes a dry valley with characteristics of a cold desert. Snowfall in the area varies from less than 1 m to as much as 6 m, with higher altitudes experiencing greater amounts. In winter, the temperature at Keylong ranges from -10°C to $+10^{\circ}\text{C}$ and in summer, the temperature ranges from 7° to 23°C ⁵⁶.

Geology

The study area is situated near the Tandri syncline and Shikar Beh nappe of Haimanta formation that has thick sequence of unmetamorphosed to less metamorphosed sedimentary rocks, from the Precambrian-Cambrian era (Fig. 2). The Tandri Syncline, is a large-scale synformal fold containing Permian to Jurassic Tethyan metasediments, formed during a NE-directed nappe stacking event and characterized by an overturned limb with thrust imbricates⁵⁷. The Tandri Group represents a sequence of predominantly carbonate rocks that are underlain by chlorite phyllite and overlies Precambrian-Eocambrian Batal Formation of the Haimanta Group⁵⁸. The Shikar Beh Nappe is the Eocene aged thrusting towards the NE, reaching amphibolite facies conditions in the lower part of the Chandra basin⁵⁹. The amplitude of the Shikar Beh nappe estimated between the hinge of the Tandri syncline and frontal part located in the Baralacha La region is approximately 50 km, however the frontal part of this nappe has been eroded^{59–61}.

This region is situated between South Tibetan Detachment System (STDS) in the northeast and Main Central Thrust (MCT) in the southwest (Fig. 2). The greenschist to granulite grade metamorphic rocks along with migmatites are situated between the MCT and the STDS throughout the Himalaya. These exposures are separated from the overlying low-grade to unmetamorphosed Tethyan Himalayan Sequence (THS) by segments of the STD system, locally referred to as the Sangla detachment and Zaskar shear zone⁵⁷.

Data used

In this study, we used ESA Sentinel-1 images for the analysis of deformation pattern and ERA5 data for climatological observation. The C-band interferometric synthetic aperture radar (InSAR) data obtained from the Copernicus Sentinel-1 mission, launched by the European Space Agency (ESA) in 2014. The Data are downloaded from NASA's Alaska Satellite Facility Data Archive and Communications Center (ASF-DACC). The Interferometric wide (IW) swath mode and VV polarization mode are used in this study. The spatial resolution is 5 m in the range direction and 20 m in the azimuth direction. We downloaded the Sentinel data from April 2022 to September 2023 along the ascending orbit track as proposed by⁶². Using this dataset, we generated interferometric pairs with 4 nearest acquisitions in time and the highly noisy interferogram was dropped from the analysis. The main sources of data noise in interferogram pairs are vegetation, heavy monsoon and snow

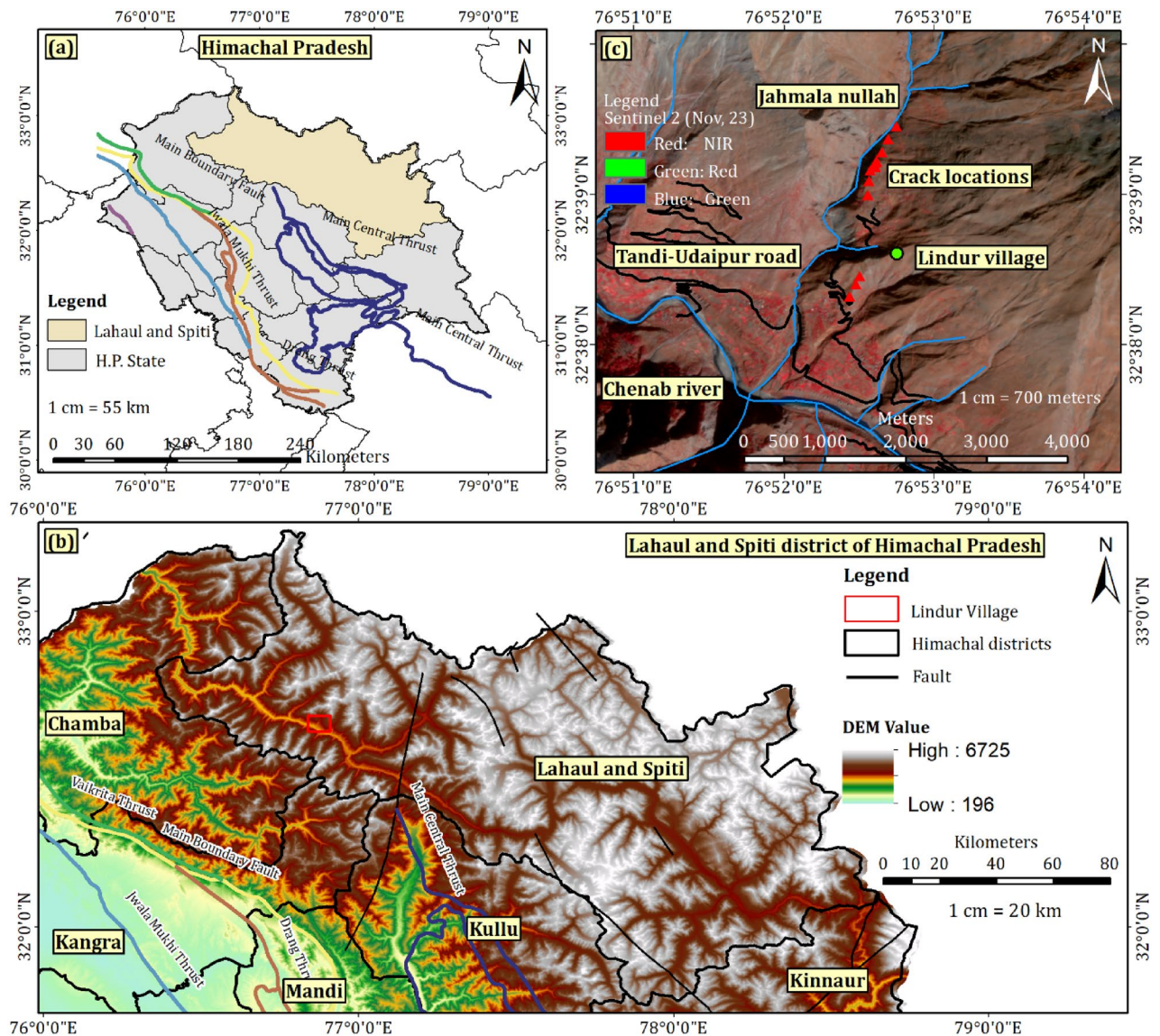


Fig. 1. The study area map (a) Himachal Pradesh administrative boundary (b) Elevation map of the Lahaul and Spiti District (Image source: SRTM DEM) (c) Crack Location in Lindur village (Image Source: Sentinel 2 (Data acquisition: 3 November 2023), ESA Copernicus) (This map is generated using ArcGIS Pro 3.2.2, Licensed to School of Civil and Environmental Engineering, IIT Mandi).

cover. However, in our study area the primary correlation noise is due to the thick snow cover during winters. The highest phase noise was observed during the winter season (October–March), and for those interferograms with longer temporal baselines as suggested by⁶². Considering the high correlation noise during the winter we could not perform the seasonal displacement over the study area. Therefore, we analysed the interferogram covering a time span of seven months, from April 2022 to September 2022 as presented in Table 1.

The study also analyzed climatic influences related to the permafrost degradation over the study area using the ERA5 reanalysis data from the European Centre for Medium-Range Weather forecasts (ECMWF) from 1950 to 2024. ERA5 offers hourly climate variables at $0.25^{\circ} \times 0.25^{\circ}$ spatial resolution⁶³. The ground observation daily temperature data at Keylong, Lahaul and Spiti was obtained from October 2022 to October 2023 to validate the ERA5 data. Climatic variables such as temperature and precipitation were used in this study to investigate potential correlations between climatic factors and observed surface deformation.

Methodology

The methodology of this study is broadly divided into four sections (Fig. 3). In the first section, we have collected data from various sources. In the second stage ISCE framework was used to compute the interferogram stack. In third stage the displacement time series map was obtained using time series analysis. Finally in the fourth stage a permafrost probability map is prepared by considering rock glaciers as a proxy for the presence of permafrost and climatological data are used to observe potential correlations with the ground deformation rate.

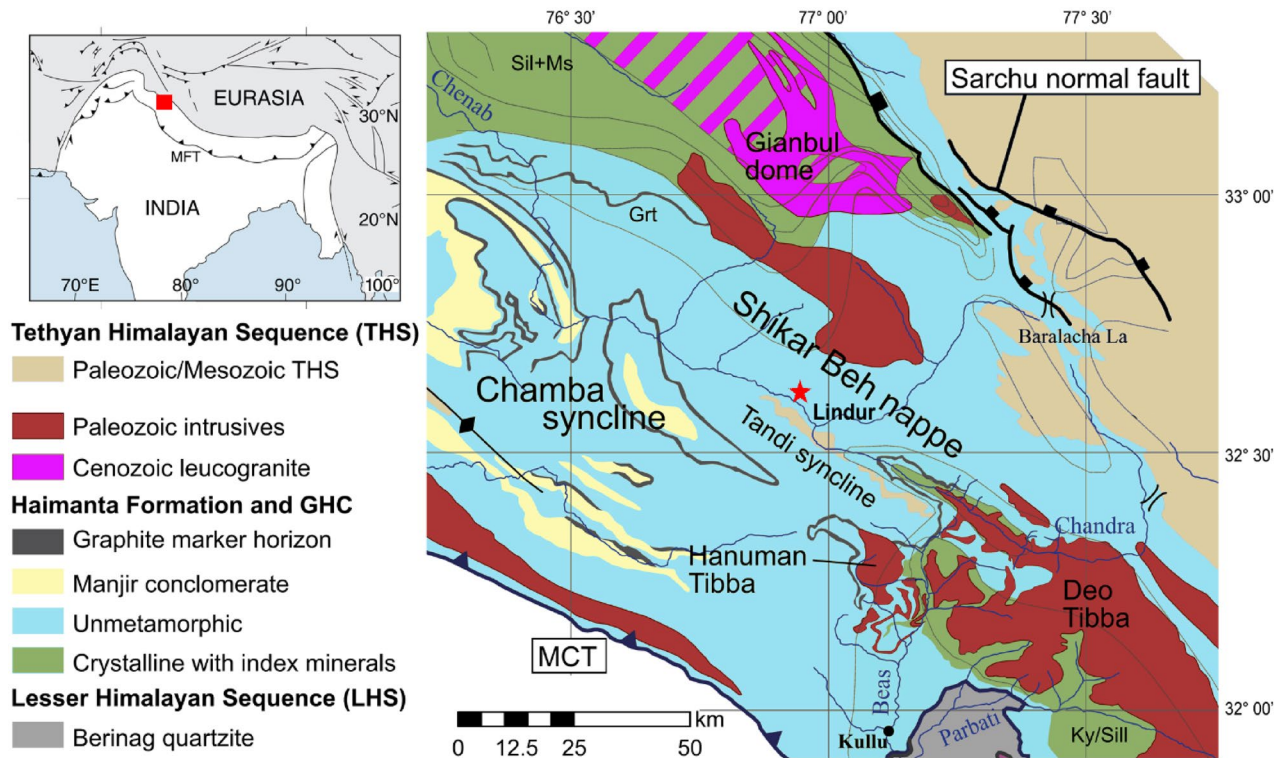


Fig. 2. Geological Map of the NW Himalaya showing the location of Lindur village situated in the Haimanta formation and its tectonic settings (Modified from⁵⁹).

SAR sensor	Path	Orbit	Acquisition date	Reference/Secondary	Bprep(m)	Source
Sentinel 1 SLC	27	43,849	27-Jun-22	Reference	0	Alaska Satellite Facility (ASF)
		42,624	04-Apr-22	Secondary	-14.45	
		43,149	10-May-22	Secondary	20.2	
		42,799	16-Apr-22	Secondary	12.62	
		42,974	28-Apr-22	Secondary	-41	
		43,674	15-Jun-22	Secondary	110.16	
		43,324	22-May-22	Secondary	34.15	
		43,499	03-Jun-22	Secondary	-70.59	
		44,024	09-Jul-22	Secondary	-54.1	
		44,199	21-Jul-22	Secondary	-51.93	
		44,374	02-Aug-22	Secondary	-33.44	
		44,549	14-Aug-22	Secondary	20.08	
		44,724	26-Aug-22	Secondary	65.31	
		44,899	07-Sep-22	Secondary	-140.11	
		45,074	19-Sep-22	Secondary	98.56	

Table 1. Sentinel 1A imagery acquisition date, orbit, path, and perpendicular base line.

Permafrost mapping

To quantify the probability of permafrost occurrence in the selected study area, this study utilized the most effective machine learning model suggested by¹³. The methodology for mapping permafrost using rock glaciers as proxies through a random forest machine learning model by integrating climatological and topographical variables to map permafrost occurrence. The process begins with the collection of rock glacier inventories generated through onscreen visual interpretation and digitization of rock glacier boundaries. We selected only intact rock glaciers to increase the model performance and probability of permafrost existence. Furthermore, 70% of the rock glaciers were considered in the training samples, and the remaining 30% were considered in the testing samples. Similarly, the key climatological and topographical variables are derived from the available remote sensing data. This study selected eight conditioning factors, such as slope, aspect, elevation, curvature, mean annual land surface temperature (MA-LST), the mean annual normalized difference snow index (MA-

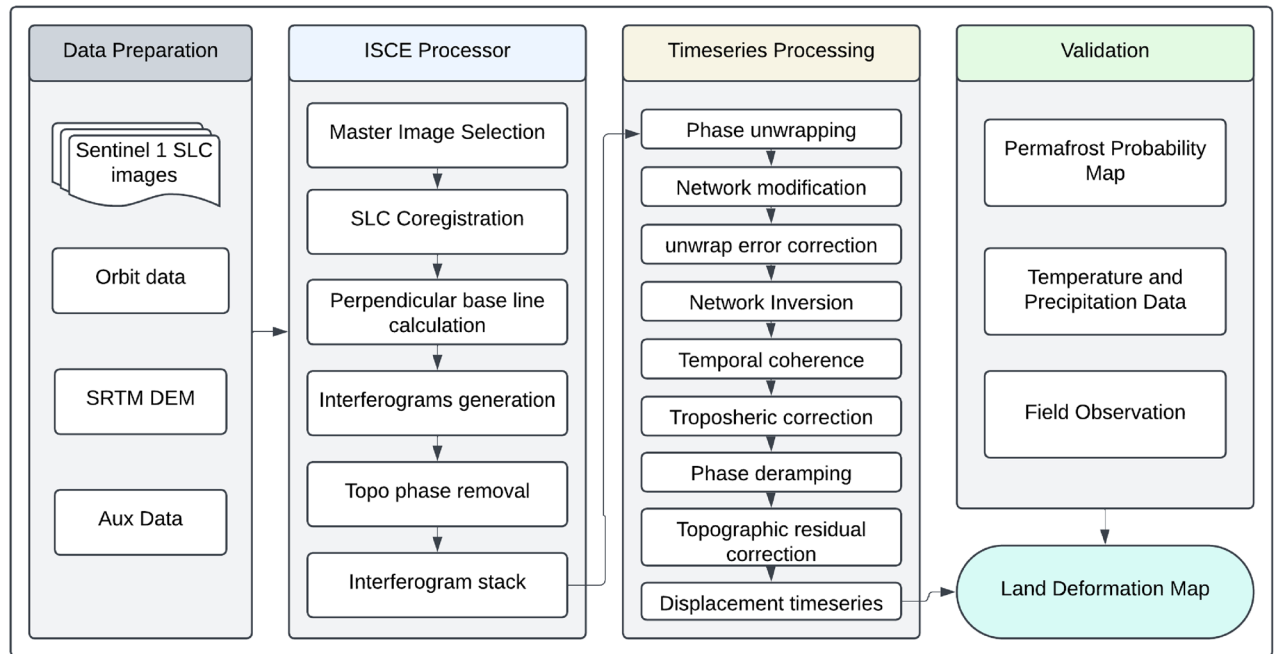


Fig. 3. Methodology chart showing the MT-InSAR technique by EZ-InSAR for land deformation map and validation using permafrost probability map, temperature data, precipitation data, and field observations.

NDSI), the mean annual normalized difference water index (MA-NDWI), and lithology, for permafrost mapping. The RF algorithm is a robust and nonlinear ensemble machine learning algorithm trained on labeled datasets to predict permafrost occurrence over the study area. The model's performance was assessed through the area under the curve (AUC-ROC).

Time series deformation mapping

We used EZ-InSAR, an open-source toolbox for deformation mapping in the study region. The workflow for time series analysis is divided into three different blocks: (i) InSAR data preparation, (ii) ISCE processing, and (iii) time series analysis. These workflow blocks are accessible within the toolbox through three main sections in the user interface. The toolbox comes with a graphical user interface (GUI), has a progress bar for each InSAR processing step and shows the progress status and next steps during the data processing.

InSAR data preparation

Sentinel-1 InSAR data were searched and downloaded using the SAR data preparation module within the EZ-InSAR toolbox. A KML file of the selected study area was exported from Google Earth to define a search zone for the data search. After defining the study area, filtering keywords such as satellite name, path number, satellite direction (ascending or descending), and the desired time span were applied to search the Sentinel-1 SAR archive via the Alaska Satellite Facility (ASF) API. Once the provided data list has been verified, the EZ-InSAR toolbox can automatically download the SAR data. Prior to the interferogram computation, a DEM encompassing the study area was downloaded. For this purpose, the Copernicus 1 arc-second DEM was downloaded from Amazon Web Services in GeoTIFF format, and the spatial resolution of the DEM was 30 m.

ISCE processing

The InSAR Scientific Computing Environment (ISCE) framework developed by the Natural Geohazard Research Group at University College Dublin (UCD) under Eoghan Holohan, was used for interferogram generation and phase unwrapping^{64,65}. The ISCE software package is a hierarchical package that combines shell and python scripts, is specifically designed to perform several tasks related to interferogram generation. These include creating a stack of coregistered SLC images, generating interferogram stacks without phase unwrapping and producing stacks of unwrapped interferograms. The interferometry module of EZ-InSAR provides an option to choose between “SLC stack” or “Unwrapped interferogram stack”, depending on the user requirements, whether the user wants to perform the time series analysis via the StaMPS or MintPy time series processor. In this study, we selected the Unwrapped Interferogram stack option for time series analysis in the MintPy processor. EZ_InSAR provides eleven steps to generate the unwrapped interferogram. The steps are *unpack_topo_reference*, *unpack_secondary_slc*, *average_baseline*, *fullBurst_geo2rdr*, *fullBurst_resample*, *extract_stack_valid_region*, *merge_reference_secondary_slc*, *generate_burst_igram*, *merge_burst_igram*, *filter_coherence* and *unwrap*.

SBAS time series analysis

The workflow for InSAR time series analysis in this study follows the Miami InSAR time series software in Python (MintPy) approach to convert unwrapped interferogram stacks into displacement time series⁶⁶. This workflow consists of two main stages: (i) correcting unwrapping errors and inverting the raw phase time series and (ii) adjusting for phase contributions from various sources to derive the displacement time series. The process begins with initializing the MintPy processor for time series analysis. The phase-unwrapped interferograms generated by the ISCE framework are registered to a common SAR acquisition for Earth curvature and topographic corrections. To address outliers caused by unwrapping errors in coherent pixels, a network modification step is employed as an optional feature in MintPy. This step eliminates interferograms with spatially averaged coherence values below a predefined threshold value. Although the processor provides other approaches for network modifications, such as thresholds for temporal and spatial baselines, the maximum number of connections per acquisition and the exclusion of precise interferograms from a particular acquisition. Similarly, the reference point was selected on the basis of the conditions suggested by⁶⁶. The reference point is situated in an area based on prior field verification and following three conditions: the point should be in a coherent area, in an area with low atmospheric disturbance and at the same elevation as the area of interest.

Furthermore, to ensure temporal consistency in a redundant interferogram network, the integer ambiguities of unwrapped interferometric phases can be mathematically represented for each pixel as follows⁶⁶:

$$CU + (C\Delta\varphi - \text{wrap}(C\Delta\varphi)) / (2\pi) = 0 \quad (1)$$

Here, C is a $T \times M$ design matrix that accounts for all possible interferogram triplets, and U is the $M \times 1$ vector representing the integer cycle numbers necessary for maintain phase consistency. where $\Delta\varphi$ denotes the unwrapped interferometric phase and wrap is the operation used to wrap the phase to its principal value within $[-\pi, \pi]$. This equation can sometimes be ill-posed when $T < M$ (fewer triplets than interferograms), meaning that a unique solution is not guaranteed. Regularization techniques are employed to overcome this limitation, favoring solutions that are both sparse and small in magnitude. This approach utilized least squares optimization, commonly known as the least absolute shrinkage and selection operator (LASSO). The LASSO optimization objective function is expressed as follows:

$$\hat{U} = \text{argmin} \| CU + C\Delta\varphi - \text{wrap}(C\Delta\varphi) / (2\pi) \|_2 + \alpha \| U \|_1 \quad (2)$$

where the α regularization parameter and $\alpha = 0.01$, determined through simulation or empirical testing, balance the trade-off between the L1 and L2-norm terms.

After solving for \hat{U} , the corrected unwrapped interferometric phase is computed as:

$$\Delta\varphi_c = \Delta\varphi + 2\pi \cdot \text{round}(\hat{U}) \quad (3)$$

Here, the round operator rounds \hat{U} to the nearest integer, ensuring consistency in the phase data. The methods improve the efficiency of phase unwrapping by mitigating inconsistencies, specifically in areas with sparse coherence and following advanced regularization approaches⁶⁷. Similarly, the raw phase time series is determined by minimizing the residual interferometric phase $\Delta\varphi_\varepsilon$. The temporal coherence γ_{temp} is subsequently calculated via the following equation⁶⁸:

$$\gamma_{temp} = \frac{1}{M} |H^T \exp[j(\Delta\varphi - A\hat{\varphi})]| \quad (4)$$

Here, j represents the imaginary unit, and H is an $M \times 1$ column vector filled with one. A denotes a threshold for temporal coherence, which is applied to identify pixels suitable for reliable network inversion. The coherence threshold was iteratively varied between 0.4 and 0.7 to obtain the most optimal value. We observe that when the value is less than 0.7 there was high noise in temporal coherence near the river valley. Therefore, we kept the coherence threshold of 0.7 to get the reliable pixel. The location of reference point with the geo temporal coherence value show in the supplementary fig. S1.

Tropospheric delay correction was conducted using global atmospheric models (GAMs). The relative double path tropospheric delay at t_i between a specific pixel p and a reference pixel is expressed as follows:

$$\hat{\varphi}_{tropo}^i(p) = (\delta L_p^i - \delta L_p^1) \frac{4\pi}{\lambda} - (\delta L_{ref}^i - \delta L_{ref}^1) \frac{4\pi}{\lambda} \quad (5)$$

Here, $i \in [1 \dots N]$, δL_x^i represents the integrated absolute single path tropospheric delay at t_i for pixel x in meters, measured in the satellite line-of sight (LOS) direction (with δL_p^1 for t_1), and λ is the radar wavelength in meters. Climatic datasets such as ERA-5 and ERA-Interim from ECM-EWF, NARR from NOAA and MRR from NASA were utilized via PyAPS software^{69,70}.

The topographic phase residual due to DEM errors is estimated on the basis of its proportional relationship with the temporal baseline over time⁷¹. Traditional methods typically employ a cubic temporal deformation model, which is unable to accurately capture high-frequency displacement signals caused by events such as earthquakes, volcanic eruptions and landslides. To address this limitation, Yunjun et al.⁶⁶ included step functions, following the method provided by⁷², allowing for permanent displacement offsets and general polynomial modeling with a user-defined polynomial order (N_{poly}). The DEM error (z_ε) for each pixel is modeled as:

$$\hat{\varphi}^i - \hat{\varphi}_{tropo}^i = \left(\frac{B_{\perp}^i}{r \sin(\theta)} z_{\varepsilon} + \sum_{k=0}^{N_{poly}} c_k (t_i - t_1)^k / k! + \sum_{l \in I_s} s_l H(t_i - t_l) \right) \frac{-4\pi}{\lambda} + \varphi_{resid}^i \quad (6)$$

where $i \in [1, \dots, N]$, B_{\perp}^i is the perpendicular baseline at time t_i relative to the reference time t_1 . r is the slant range, and θ is the incidence angle. $H(t_i - t_l)$ is a Heaviside step function centered at specific times t_l , corresponding to displacement jumps. z_{ε} , c_k and s_l are unknown parameters determined by minimizing the L^2 norm of the residual phase time series $\varphi_{resid} = [\varphi_{resid}^1, \dots, \varphi_{resid}^N]^T$. Examples of design matrices and numerical solutions using least square estimation are provided in the supplementary section of⁶⁶.

Furthermore, the residual phase ($\hat{\varphi}_{resid}^i$) derived from the DEM error equation as a byproduct serves as an indicator of the noise level in the InSAR time series. The noise level for each SAR acquisition is quantified by computing the root mean square (RMS) of the residual phase, expressed as:

$$RMS^i = \sqrt{\frac{1}{N_{\Omega}} \sum_{p \in \Omega} \left(\hat{\varphi}_{resid}^i(p) \cdot \frac{\lambda}{-4\pi} \right)^2} \quad (7)$$

where $i = [1, \dots, N]$, which represents the SAR acquisition index. where $\hat{\varphi}_{resid}^i(p)$ is the residual phase for pixel p at time t_i . Ω is a set of reliable pixels chosen based on temporal coherence during the network inversion process. N_{Ω} is the total number of reliable pixels in Ω . λ is the radar wavelength. Since long-wavelength phase components in $\hat{\varphi}_{resid}^i$ are typically difficult to assess precisely, noise evaluation focuses on short-wavelength phase variation⁶⁶. To isolate short wavelength noise, a quadratic phase ramp is removed from the residual phase of each acquisition before calculating the Root Mean Square Error (RMSE)^{66,73,74}. After calculating the RMSE, we excluded the noisy SAR data and selected the best optimal reference date. Furthermore, the average velocity v is calculated as the slope of the best fitting line to the displacement time series using the equation $\varphi_{dis}^i \cdot \frac{\lambda}{-4\pi} = v \cdot t_i + c$, $i = 1, \dots, N$, where c is an unknown offset constant.

ERA-5 analysis

The ERA-5 reanalysis datasets were obtained from the ECMWF⁷⁵. These datasets were utilized to analyze the temperature and precipitation trends in the study area. The focus was on understanding how air temperature and precipitation patterns along with their combined effects contribute to crack formation. We used ERA5-Land Daily Aggregated data, which has a spatial resolution of 11 km and spans from 1950 to 2024, to produce time series plots for temperature and precipitation. To understand the historical trends, this study used the Mann-Kendall test, linear regression and Theil-Sen analysis^{76–80}.

Results

InSAR deformation

Using the MT-InSAR technique, we obtained the surface deformation area in the selected study region. The displacement results span from April 2022 to September 2022. The observed ground movement velocities are shown in Fig. 4a. The velocity map highlights the region with significant surface movement, expressed in centimeter per year (cm/year). The velocity map clearly indicates substantial surface displacement of 7.914 cm/year in the toe region of the elongated rock glacier present in that area. The negative velocity values indicate movement toward the sensor (i.e., uplift), and positive values indicate movement away from the sensor (i.e., subsidence). The subsidence area is most likely linked with the thawing of permafrost or soil compaction due to the melting of underground ice. In contrast to the subsidence area, the neighboring area experiences surface displacement close to zero. The transection line from the top of the rock glacier to the river showing an increasing subsidence rate from 0 to 7.914 cm/year (Fig. 4b). Furthermore, the standard deviation map (Fig. S2a) quantifies the reliability of the measurements, showing higher uncertainties of 0.02 m/year. Uncertain areas are present along the river valley and areas with steep terrain, which is caused mainly by low radar signal coherence. Lindur village, which is situated in a region with lower standard deviation values, has robust and reliable displacement estimates.

The intercept map representing the initial displacement values at the start of the observation period shows minor variation ranging from approximately -0.02 to 0.01 m (Fig. S2b). The residual map represents signal noise after applying the linear model to the time series data, revealing that the residue is less than -0.01 m, which indicates that the linear model effectively captures the deformation trends (Fig. S2c). Similarly, the obtained intercept value map reveals low uncertainties (< 0.003 m) across most of the study area (Fig. S2d). The highest intercept value was observed in the area where the velocity was at its maximum. Furthermore, the spatiotemporal evolution of deformation patterns across the village is shown in Fig. 5. The time series map shows that the displacement rapidly increases from the summer season until the beginning of winter, indicating that subsidence is attributed to the thawing of permafrost during the summer season.

Permafrost area

The permafrost probability map for the study area was prepared via the random forest (RF) machine learning method. The obtained probability values of permafrost occurrence were further divided into three classes, namely, low, moderate, and high, on the basis of the natural break classification (Fig. 6b). The map shows that areas with elevations greater than 3800 have a probability of permafrost occurrence. There is very little permafrost in the habitat region of the village. Similarly, the agricultural area and the NE region of the village have the

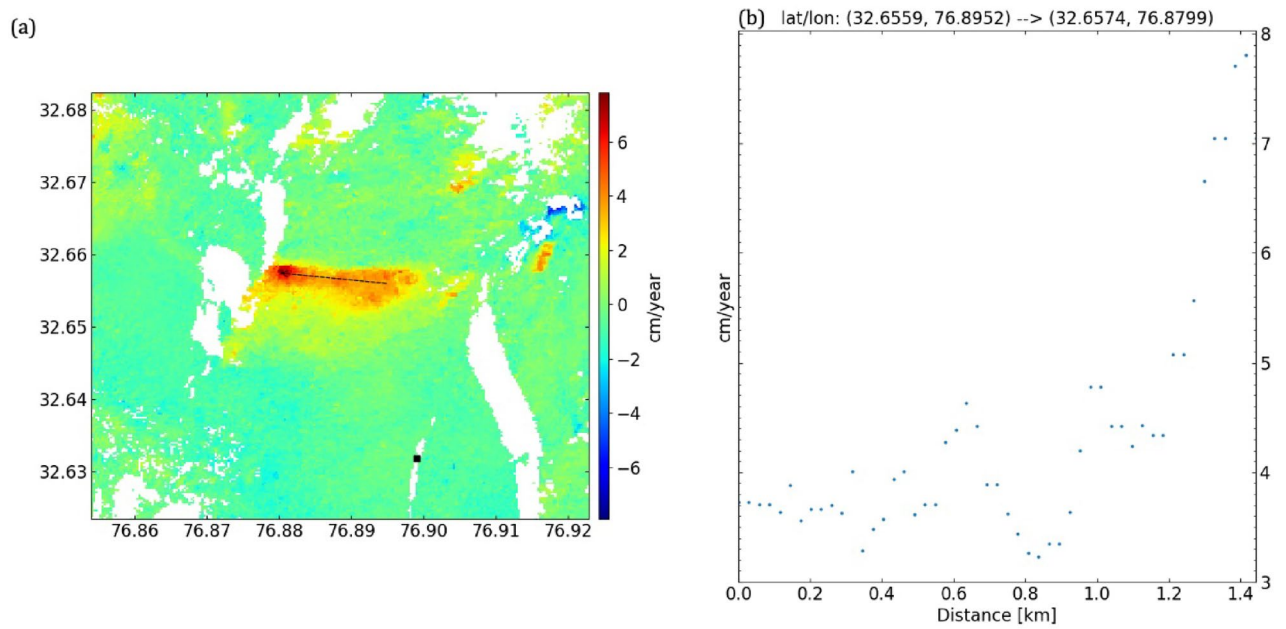


Fig. 4. (a) Map showing the observed permafrost deformation rates in cm/year. (b) Displacement rate variation along the transection line extending from the rock glacier to the river.

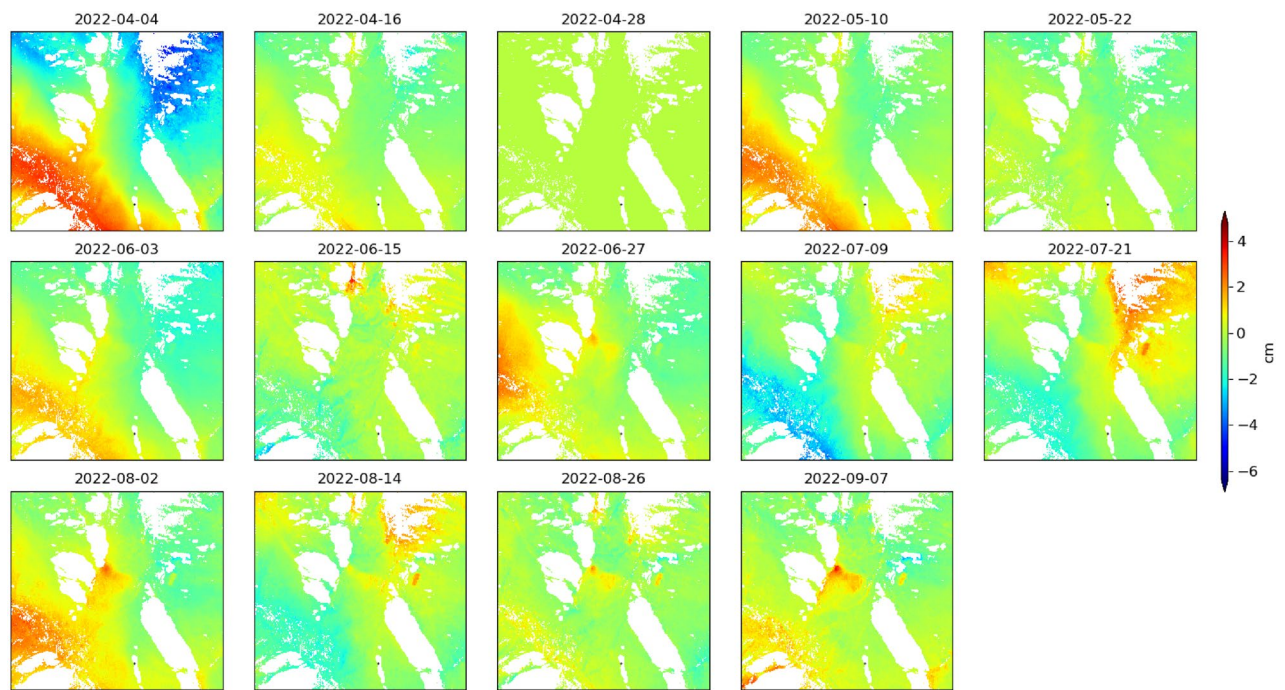


Fig. 5. Displacement time series observed from April 2022 to September 2022 over the study area, showing temporal variation in surface movement.

highest probability of permafrost occurrence. On the other hand, as we considered rock glaciers as proxies for permafrost presence, the results revealed very high permafrost occurrence over rock glaciers and adjacent areas. The evaluation of the model for permafrost modeling over the study region revealed an AUC-ROC score of 0.93. Furthermore, the high probability zone of permafrost area was compared with the land deformation map and found that the high probability zone are associated with the high deformation zones (Fig. 6a).

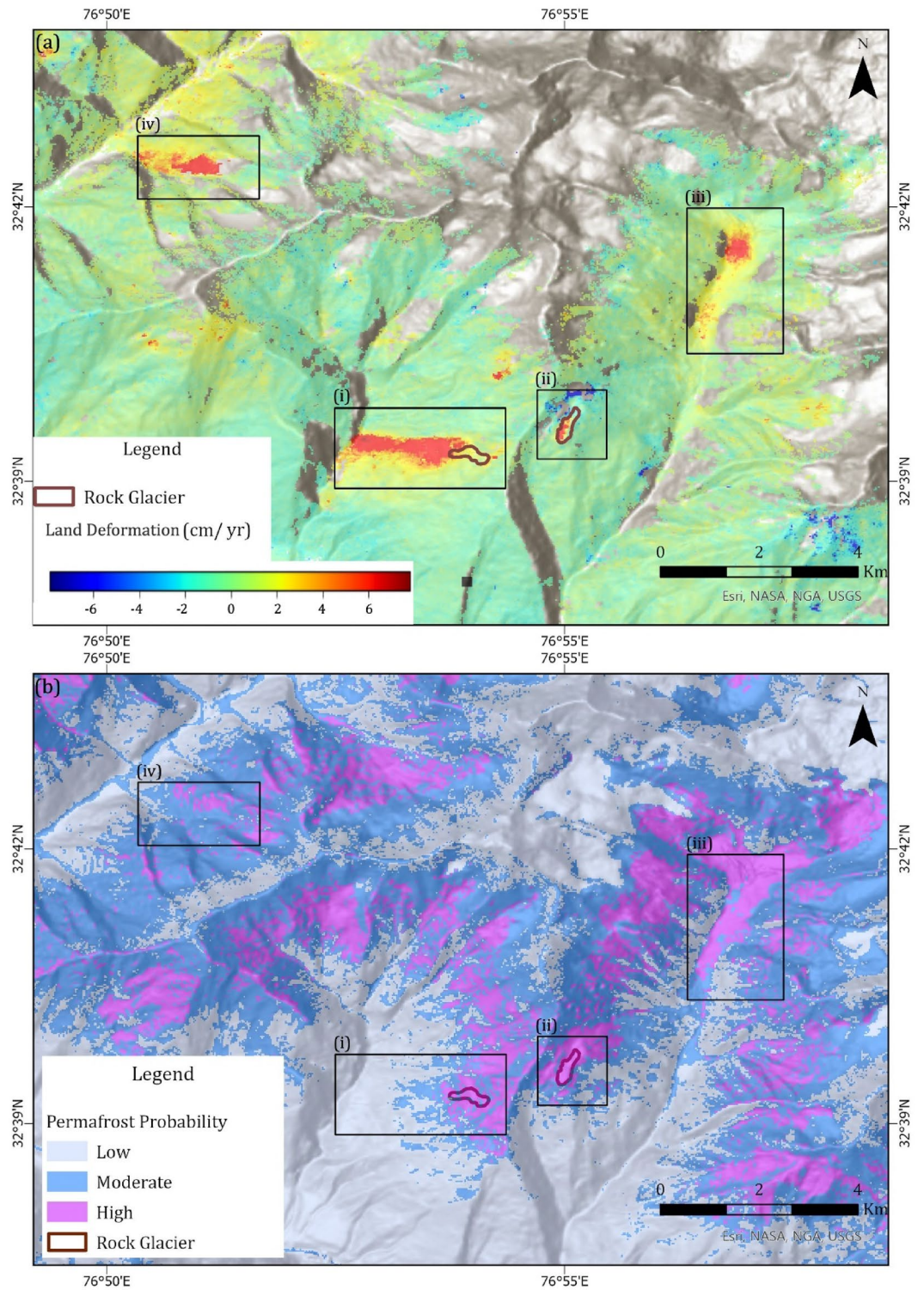


Fig. 6. (a) Map showing Land deformation rate (cm/year) over Lindur village and nearby area, black boxes representing significant deformation regions (i) Lindur village (ii) Rock glacier (iii) Talus slope with high permafrost probability (iv) area with moderate permafrost probability. Rock glacier boundaries are shown in red colour. (b) Permafrost probability map with low, moderate, and high probability of permafrost. The black boxes represent deformation areas with a significant deformation rate that gives a spatial relationship between deformation and permafrost occurrence.

Climatological observations

Lindur village is located in a remote region devoid of an operational weather station. The nearest weather station is situated in Keylong around 30 km away from the study area. The ground observation daily temperature data could only be obtained for one year i.e. from October 2022 to 2023. Due to short temporal availability of ground observation data ERA5 data was used to analyze the temperature and precipitation trend over the region. Before carrying out the detailed analysis of ERA5 data, it was validated from the ground observation data. It was observed that the coefficient of determination between the ERA-5 data and the observed data having 357 data points was 0.82 which indicates a strong correlation. Furthermore, the root mean square error (RMSE) and mean absolute error (MAE) were calculated as 4.15 and 3.17 °C, respectively (Fig. 7a,b). It is interesting to observe that ERA5 tends to underestimate the actual temperature data, but it follows a similar trend as that of observed data. Hence for long term temperature variation analysis ERA5 data was used.

Upon analyzing the annual average air temperature trend along with its 10-year rolling average trend line, it is evident that the air temperature has steadily increased over time. In 1950, the annual average air temperature was -8.40 °C, and by 2024, it had risen to -5.87 °C. We also examined both the annual average precipitation trend and the annual accumulated precipitation trend, as shown in Fig. 8a,b. In 1950, the average precipitation was 5 mm, and the accumulated precipitation was 1840 mm. By 2024, the average precipitation had decreased to 3 mm, and the accumulated precipitation had decreased to 1110 mm. Figure 8 reveals that while the air temperature has shown a consistent upward trend, precipitation has followed a cyclic pattern. Initially, the air temperature and precipitation were inversely related, and the precipitation decreased as the air temperature increased. Later, both precipitation and air temperature increased for a period, followed by a decline in both variables. In the last decade, the trend has shown that air temperature has continued to rise, whereas precipitation has continued to decrease.

For the annual average air temperature, the Mann–Kendall test indicates a significant positive trend with a statistic of 0.36 and a very small p value (0.00), confirming that the trend is statistically significant, as shown in Table 2. The linear regression analysis revealed a positive slope of 0.02, indicating that the air temperature increased by approximately 0.02 °C per year, with a p value of 0.00, further confirming the significance of this increase. The R-squared value of 0.30 means that approximately 30% of the variation in air temperature is explained by time. Additionally, the Theil–Sen analysis reveals a smaller positive slope of 0.02, corresponding to a decadal rate of +0.18 °C per decade, reinforcing the conclusion that air temperature increases over time. In contrast, the annual average precipitation showed no significant trend (Table 2). The Mann–Kendall test yields a statistic of -0.14 and a p value of 0.12, which suggests a very weak negative trend, but it is not statistically significant. Similarly, the linear regression reveals a slight negative slope of -0.01 , but with a p value of 0.09, this decrease is not statistically significant. The Theil–Sen analysis reveals an extremely small negative slope of 0.00 and a decadal rate of -0.00 mm per decade, which is practically negligible, indicating no meaningful change in the annual average precipitation. For annual accumulated precipitation, the Mann–Kendall test yields a statistic of -0.06 and a p value of 0.46, further suggesting that there is no significant trend. The linear regression shows a negative slope of -1.19 , indicating a small decrease in accumulated precipitation, but the p value (0.28) indicates that this trend is not statistically significant. The Theil–Sen analysis reveals a negative slope of -0.88 with a decadal rate of -8.85 mm per decade, suggesting a slight but insignificant decrease in accumulated precipitation over time.

Field observations

During the field traverse, several indicators of ground instability in the form of cracks were observed across the study area. We observed the orientation of the beds are towards the riverbed and sub surface ice melting water flowing to the Jahlma nala river (Fig. 9a,b). Significant numbers of cracks were observed in the agricultural field, on the wall of houses, floor of the houses, across rock glacier, and along the slope indicating a substantial surface

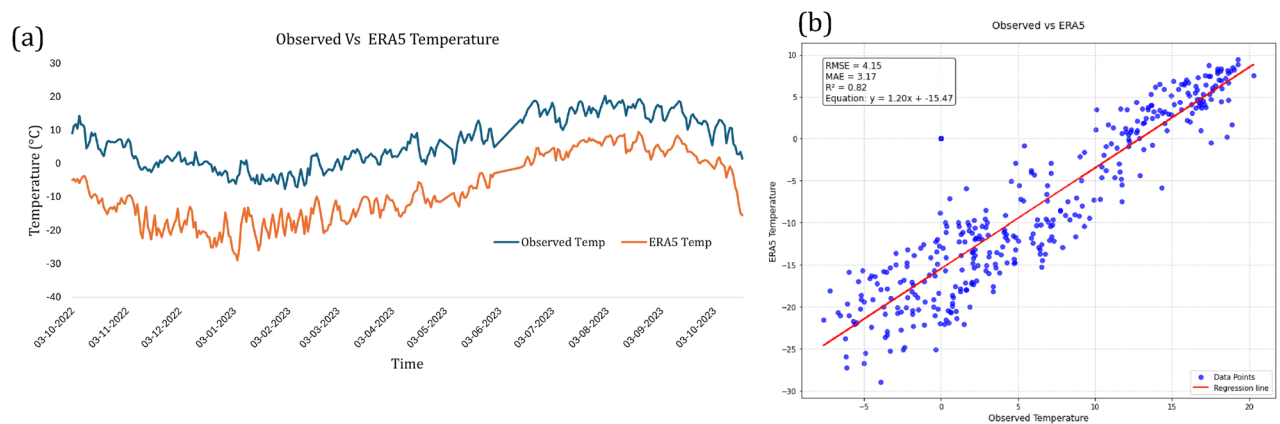


Fig. 7. Comparison of observed and ERA5 temperature data. **(a)** Time series of observed (blue line) and ERA5 (orange line) temperature (°C) from October 2022 to December 2023. **(b)** Scatter plot of observed versus ERA5 temperature (°C), with a regression line (red) fitted to the data.

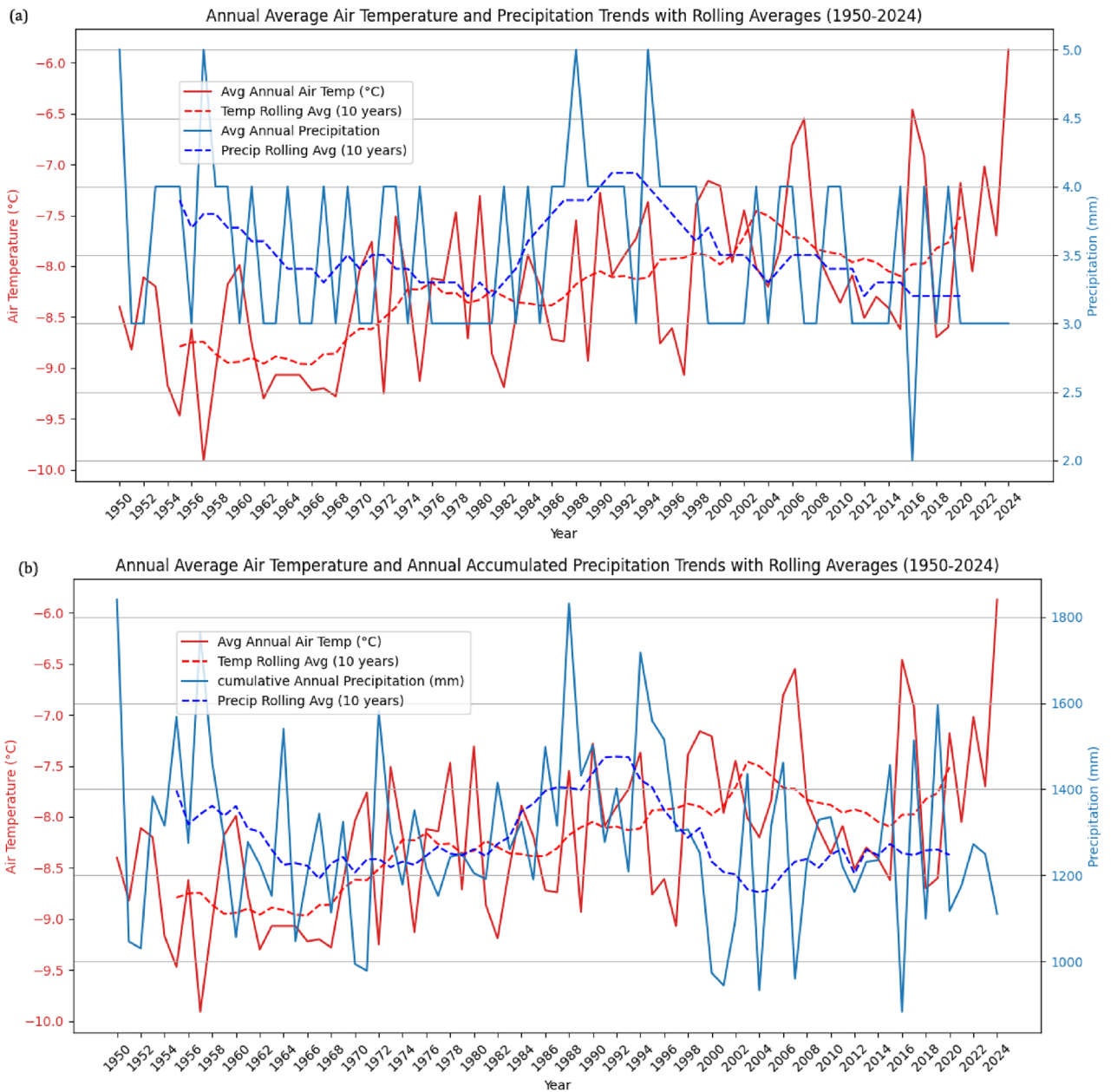


Fig. 8. Plot showing the trends of (a) Annual average air temperature (°C) and annual average precipitation (mm) from 1950 to 2024, along with their 10-year rolling average trend lines. (b) Annual average air temperature (°C) and annual accumulated precipitation (mm) from 1950 to 2024, along with their 10-year rolling average trend lines.

Tests	Metric	Annual average air temperature	Annual average precipitation	Annual accumulated precipitation
Mann-Kendall test	MK Stat	0.36	- 0.14	- 0.06
	P value	0.00	0.12	0.46
Linear regression	Slope	0.02	- 0.01	- 1.19
	P value	0.00	0.09	0.28
Theil - Sen analysis	Slope	0.02	0.00	- 0.88
	Decadal rate	0.18 °C/decade	0.00 mm/decade	- 8.85 mm/decade

Table 2. Statistical significance analysis of the annual average air temperature, annual average precipitation and annual accumulated precipitation trends was performed via the Mann-Kendall test, linear regression and Theil-Sen analysis.



Fig. 9. Field photographs showing the local geology and cracks (a) Slate bed orientation along the slope gradient (b) Subsurface ice melt water stream (c) Crack present across the rock glacier in NE direction of the village (d) Vertical cracks on the wall of a house (e) NNE-SSW trending transverse cracks observed in agricultural field (f) Drunken tree present on the slope.

movement (Fig. 9c–e). The cracks are also present in residential buildings in horizontal, vertical and diagonal patterns, indicating structural stress. The crack clearly extends over a considerable length and varies in width, indicating a complex interplay of geological forces. The crack follows the natural contours along the rooting line of the rock glacier in both elevated and relatively flat terrain. Field measurements suggest that the depth and width of the crack are greater in the northern direction than in the southern direction. The village and its surrounding terrain are situated on loose, unsorted debris material supported by a clay matrix derived from the glacier present above the village (Fig. 9a). The soft composition of the sediments forming the hillslopes renders them susceptible to swift soil erosion, especially during intense rainfall events. Additionally, displaced fences and numerous drunken trees were found, with the tilt generally oriented in the southwest direction. The drunken

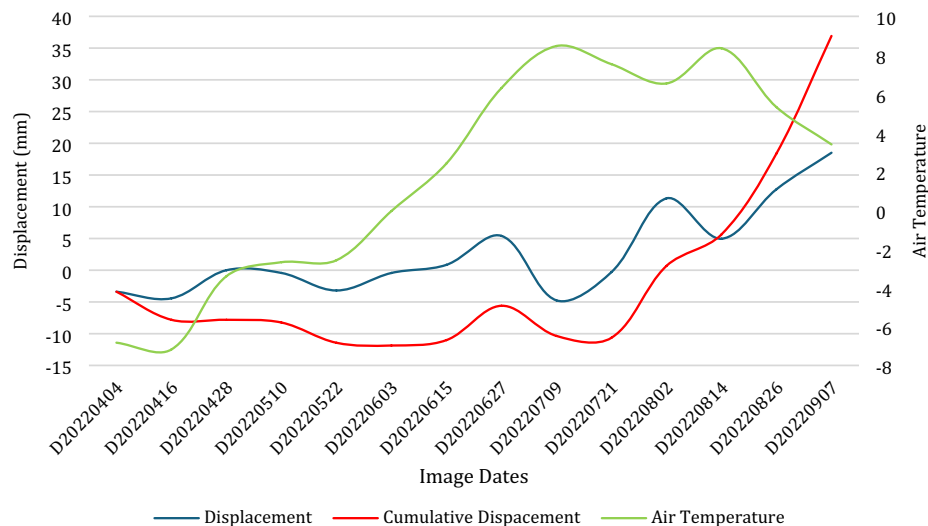


Fig. 10. Showing the displacement rate, cumulative displacement and air temperature from 04/04/2022 to 07/09/2022 over the rock glacier.

tree, loose talus derived soil and rock glacier indicating the presence of permafrost in the region (Fig. 9f). After following the major cracks present in the village area, it was observed that the major crack has subsequent parallel smaller cracks.

Discussion

Permafrost-induced land subsidence is a critical consequence of climate change and is driven by the thawing of ground ice. In recent decades, there has been a significant rise in global temperature, which is a severe concern for permafrost present in high-latitude regions. On the Tibetan Plateau, several studies have reported land degradation due to permafrost degradation^{39,52,54}. Similarly, via GPS interferometry⁸¹ reported significant interannual variations in surface deformation within the permafrost region of Alaska. Recently, in the Indian Himalayas, several studies reported that catastrophic events occurred in the Chamoli district of Uttarakhand in February 2021 with the degradation of permafrost^{14,82}. However, there is no such study available in the Indian Himalayas that aims to understand the permafrost aspects of land subsidence and slope instability.

In this study, we used multitemporal interferometric synthetic aperture radar (MTInSAR) techniques to analyze the spatial and temporal evolution of ground subsidence in Lindur village of Himachal Pradesh caused by the degradation of permafrost in this region. The use of MTInSAR has proven to be a well-established method for monitoring the slow movement of ground. By leveraging radar imagery over extended periods, this method enables the detection of subtle deformation patterns with millimeter- to centimeter-scale accuracy. Thaw-induced subsidence is largely governed by thermal degradation and hydrological changes. Rising temperatures lead to increased soil moisture, and deeper thaw depths exacerbate subsidence. The results revealed that the village experienced a high rate of land subsidence, as shown in the map, and the subsidence rate was greater than 7.9 cm/yr in the northeastern direction of the village. Similar subsidence rates are observed in areas where the permafrost occurrence probability is high. Furthermore, we observed that there is a correlation between the air temperature and cumulative displacement (Fig. 10). The cumulative displacement is increasing when the temperature is increasing.

Field observations revealed that the exposed outcrop of slate beds was oriented along the slope gradient. The alignment of beds in the direction of slopes generates a slip surface, indicating a geological setting conducive to mass wasting processes such as subsidence and landslides. The joints present in the rock create a zone of weakness within the slate beds, which reduces cohesion and increases rock susceptibility to subsidence and landslides. The glacier melt water, seepage from irrigation channels and monsoon rain contribute to the surface tension crack. Surface tension cracks are developed during the dry period after a prolonged freeze and thaw cycle. Additionally, tectonic movements in the Himalayas might influence the land subsidence in the region. Lots of papers are carried out in the eastern part of the Himalaya, mainly focusing on Manipur, Arunachal and Sikkim, in addition to eastern Tibet^{83–86}. However, such movements are not constrained in the Himachal section. The observation stations are mainly situated below the MCT line, and our study region is situated above the line. The eastern Himalayas is moving at a higher rate with a velocity of 20 mm/yr, whereas the western Himalayas is moving at a slower rate of 10 mm/yr⁸⁷. Reference⁸⁸ also reported that the GPS velocity in the Zaskar Valley was observed at a rate of 4 mm/yr. Considering the tectonic movement, micro earthquake data reported by GSI from 1900 to 2023 within the 50 km radius of the Lindur village, it was observed that 1 larger earthquake (> M 7), 2 moderate earthquakes (> M 5), and 33 small earthquakes (5 > M > 3) have occurred in the region. Additionally, the well-known devastating Kangra earthquake of 1905 occurred around 75 km (aerial distance) away from the site in the SW direction. Also, there is no major active thrust passing near the study area and this region is situated on

the southern side of STDS (South Tibetan Detachment System) on the High Himalayan slab. Metamorphism in the High Himalayan Slab, where the study area is located, is widely interpreted as the result of a regional Barrovian-type event that refers to the classic concept of progressive metamorphism under moderate pressure–temperature (P–T) conditions. It is typically associated with significant crustal shortening and thickening in the continental–continental collision orogeny, following the initial collision between the Indian and Asian plates around 54–50 Ma^{89–91}. The earliest episode of crustal thickening that has been documented is the emplacement of the Shikar Beh antiformal nappe, which is also associated with the creation of the Tandri syncline^{60,92,93}. This crustal thickening ended at 30–29 Ma as per the Monazite and garnet geochronology data^{61,91}. Afterwards the cooling of the Higher Himalayan crystalline in this area happened between ~26–20 Ma (muscovite Rb–Sr and 40Ar/39Ar ages) and ~18–10 Ma (biotite 40Ar/39Ar and Rb–Sr ages) (Schlup et al., 2011^{59,61}).

The STDS, located in the northern margin of the Higher Himalayan Sequence (HHS) in the Himalaya is a ductile to brittle shear zone that dips top-to-the-northeast-down along the northern margin of the Higher Himalayan Sequence (HHS) in the Himalaya (^{57,94}, Searle, 2010^{95–97}). Further, the STDS evolved as a prototectonic terrane boundary, that grew from the latest Neoproterozoic to uppermost Cretaceous in the Tethyan Basin thus accumulating around 10 km thick sediments. The fault system was reactivated during the Cenozoic, followed by the continuous movement from the earliest Miocene (23.68 ± 0.94 Ma) to abruptly ceasing in early Middle Miocene (13.30 ± 0.30 Ma) for nearly 10 myr⁹⁵. This indicates that the activity along the STDS has ceased in the Neogene and the quaternary period. Thus, it seems that the effect of neo-tectonic movement in the deformation observed in this location seems very less.

The relationship between climate change and permafrost degradation is a critical process with widespread environmental and societal impacts. Climate change, driven by rising global temperatures causes permafrost to thaw. As temperature increases the active layer of permafrost thaws, and deeper frozen layers begin to melt leading to land degradation⁹⁸. This degradation leads to significant landscape change including land subsidence and slope instability⁹⁹. To understand the impact of local climatic conditions over the years, this study utilized temperature and precipitation data obtained from ERA-5. The analysis revealed that the annual temperature in the study area is rising at a rate of 0.02 °C/year. Although precipitation also showed a decreasing trend, the rate of decline was not statistically significant. Similar findings regarding temperature increases were reported by¹⁰⁰. In a related study¹⁰¹ found a significant decrease in annual average snowfall in Keylong and Udaipur, with rates of 11.1 cm/yr and 5.3 cm/year, respectively, from 1982 to 2017 and 1975–2016. They also reported a slight increase in average annual temperature at a rate of 0.0006 °C per year. The rise in temperature and decrease in precipitation in the form of snow and rain are the primary reasons for the permafrost thaw and melting of ground ice leading to ground subsidence in this region. Furthermore, as precipitation is most prominent during the monsoon season in the Indian Himalayas, which lasts from June to the end of September, we analyzed the monthly average precipitation trends for June, July, August, and September (Fig. S3). Similarly, we examined the monthly average air temperature trends for the same months (Fig. S4). Both figures visualize the 4-year and 10-year rolling average trends for precipitation and air temperature, providing a clearer picture of the short term and long-term patterns in these variables. Precipitation trends reveal a clear and statistically significant increase in June, suggesting more rainfall at the start of the monsoon season. However, July to September does not show significant trends in precipitation (Fig. S3). Air temperature trends show consistent and significant warming during June, July, and August, indicating a rise in temperature during the monsoon months, whereas September shows no significant increase (Fig. S4), suggesting stabilization at the end of the monsoon.

Conclusion

In this study, we analyzed the cause of land subsidence in Lindur village of Himachal Pradesh. For this purpose, we use the SBAS-InSAR technique with Sentinel-1A images from April 2022 to September 2022. The results revealed significant subsidence rates ranging from –6.8 cm/year to 7.9 cm/year. High subsidence areas are dominated by areas where the probability of permafrost occurrence is high, conversely the negative deformation rates in high-elevation regions indicate snow accumulation. The cumulative displacement over the seven months was 16 cm, showing a significant land deformation in the region. From the observation of the deformation pattern and its association, it is evident that the area proxies to permafrost such as rock glaciers and talus slope have a high value of deformation rate indicating the degradation of permafrost in the study area.

Furthermore, the study depicted that a combination of climatic and geological factors influences land subsidence in Lindur village. The analysis of the ERA-5 temperature and precipitation data revealed a significant increase in the annual temperature at a rate of 0.02 °C per year. Similarly, a reduction in snow accumulation in winters and increase in monsoon precipitation was over the region. The rise in temperatures leads to the melting of permafrost is a primary reason for subsidence. Increase rain fall in monsoon exacerbates permafrost melting due to its higher thermal conductivity and percolation of water to the ground. Moreover, field observations indicated that the slate beds are orientated along the gradient slope, jointed rock formations and rock glacier movement further accelerated the ground deformation and slope instability.

This study highlights the importance of more detailed studies into the interaction of climatic, geological and hydrological factors that drive permafrost thaw and land subsidence in the Indian Himalayas. The quantified deformation rates and identified vulnerable areas provide crucial information for developing targeted mitigation strategies and early warning systems. Finally, these measures can contribute to improved disaster preparedness and risk management for the residents of mountainous regions.

Limitations and future scope

This study provides a comprehensive understanding into permafrost melt-induced subsidence in the study region despite over limitations. One of the primary limitations of the study is that it is considered only a single season

from April to September 2022. This restricts the analysis of seasonal variations in permafrost melt-induced subsidence. The decision to consider only a single seasonal variation is due to the limited ground penetration capability of C-band SAR data. C-band SAR data has shorter wavelengths and limited penetration ability through snow reduces the temporal coherence. This limitation affects the accuracy of deformation measurements^{85,86,102}. Another limitation is the absence of below-ground temperature data over the study region and the absence of subsurface validation, such as the use of ground penetrating radar (GPR). The use of ground observation data and the use of the GRP could increase the reliability of deformation mapping by providing critical subsurface insights.

To address these limitations, future research in the Himalayas should focus on multiple seasonal and interannual analyses to provide a comprehensive understanding of how permafrost melts and how subsidence evolves over time. The incorporation of L-band SAR data would help overcome penetration challenges during snow cover periods and enhance deformation mapping accuracy. Additionally, integrating GPR and below-ground temperatures can provide critical validation of SAR-based observations.

Data availability

Data and the codes used will be made available by the corresponding author upon reasonable request.

Received: 28 January 2025; Accepted: 23 May 2025

Published online: 02 June 2025

References

1. Biskaborn, B. K. et al. Permafrost is warming at a global scale. *Nat. Commun.* **10**(1), 264. <https://doi.org/10.1038/s41467-018-08240-4> (2019).
2. Dobinski, W. Permafrost. *Earth Sci. Rev.* **108**(3), 158–169. <https://doi.org/10.1016/j.earscirev.2011.06.007> (2011).
3. Riseborough, D., Shiklomanov, N., Eitzelmüller, B., Gruber, S. & Marchenko, S. Recent advances in permafrost modelling. *Permafrost Periglac. Process.* **19**(2), 137–156. <https://doi.org/10.1002/ppp.615> (2008).
4. Obu, J. How Much of the Earth's Surface is Underlain by Permafrost?. *J. Geophys. Res. Earth Surf.* <https://doi.org/10.1029/2021JF006123> (2021).
5. Zhang, T., Barry, R. G., Knowles, K., Heginbottom, J. A. & Brown, J. Statistics and characteristics of permafrost and ground-ice distribution in the Northern Hemisphere 1. *Polar Geogr.* **23**(2), 132–154. <https://doi.org/10.1080/10889379909377670> (1999).
6. Gorbunov, A. P. Permafrost investigations in high-mountain regions*. *Arct. Alp. Res.* **10**(2), 283–294. <https://doi.org/10.1080/00040851.1978.12003967> (1978).
7. Gruber, S. et al. Review article: Inferring permafrost and permafrost thaw in the mountains of the Hindu Kush Himalaya region. *Cryosphere* **11**(1), 81–99. <https://doi.org/10.5194/tc-11-81-2017> (2017).
8. Gruber, S. Derivation and analysis of a high-resolution estimate of global permafrost zonation. *Cryosphere* **6**(1), 221–233 (2012).
9. Obu, J. et al. Northern Hemisphere permafrost map based on TTOP modelling for 2000–2016 at 1 km² scale. *Earth Sci. Rev.* **193**, 299–316 (2019).
10. Singh, S. P., Bassignana-Khadka, I., Singh Karky, B. & Sharma, E. *Climate Change in the Hindu Kush-Himalayas the State of Current Knowledge* (International Centre for Integrated Mountain Development (ICIMOD), 2011).
11. Baral, P. & Haq, M. A. Spatial prediction of permafrost occurrence in Sikkim Himalayas using logistic regression, random forests, support vector machines and neural networks. *Geomorphology* **371**, 107331–107331. <https://doi.org/10.1016/J.GEOMORPH.2020.107331> (2020).
12. Khan, M. A. R. et al. Modelling permafrost distribution in western himalaya using remote sensing and field observations. *Remote Sens.* <https://doi.org/10.3390/rs13214403> (2021).
13. Mahanta, K. K., Pradhan, I. P., Gupta, S. K. & Shukla, D. P. Assessing machine learning and statistical methods for rock glacier-based permafrost distribution in Northern Kargil Region. *Permafrost Periglac. Process.* **35**(3), 262–277. <https://doi.org/10.1002/PP.2240> (2024).
14. Pandey, A. C., Ghosh, T., Parida, B. R., Dwivedi, C. S. & Tiwari, R. K. Modeling permafrost distribution using geoinformatics in the Alaknanda Valley, Uttarakhand, India. *Sustainability* <https://doi.org/10.3390/SU142315731> (2022).
15. Pradhan, I. P. et al. Evaluation of the probable permafrost distribution of Kinnaur district, Himachal Pradesh. *AGUFM* **2022**, EP42A-44 (2022).
16. Pradhan, I. P. & Shukla, D. P. Biennial analysis of probable permafrost distribution for Kullu district, North-west Himalaya using Landsat 8 satellite data. *Land Degrad. Dev.* **35**(1), 360–377. <https://doi.org/10.1002/LDR.4921> (2024).
17. Schmid, M. O. et al. Assessment of permafrost distribution maps in the Hindu Kush Himalayan region using rock glaciers mapped in Google Earth. *Cryosphere* **9**(6), 2089–2099. <https://doi.org/10.5194/TC-9-2089-2015> (2015).
18. Pradhan, I. P., Mahanta, K. K., Tiwari, N. & Shukla, D. P. Rock glaciers as proxy for machine learning based debris-covered glacier mapping of Kinnaur District, Himachal Pradesh. *Earth Sur. Process. Landforms* **49**, 3598–3619 (2024).
19. Pradhan, I. P. & Shukla, D. P. MAPPING PERMAFROST DISTRIBUTION IN THE PARVATI VALLEY, KULLU USING LANDSAT 8 DERIVED LAND SURFACE TEMPERATURE. *The International Archives of the Photogrammetry, Remote Sensing and Spatial Information Sciences/International Archives of the Photogrammetry, Remote Sensing and Spatial Information Sciences XLIII-B3-2022*, 779–784 (2022).
20. Dash, A., Pradhan, I. P., Mahanta, K. K., Tiwari, N. & Shukla, D. P. Comprehensive assessment of rock glaciers in the Himachal Himalayas: Updated inventory and labelling. *Progress Phys. Geo. Earth Environ.* **48**, 571–594 (2024).
21. Box, J. E. et al. Key indicators of Arctic climate change: 1971–2017. *Environ. Res. Lett.* **14**(4), 045010. <https://doi.org/10.1088/1748-9326/aafc1b> (2019).
22. Murton, J. B. Permafrost and climate change. In *Climate Change* (ed. Murton, J. B.) (Elsevier, 2021).
23. Romanovsky, V., Burgess, M., Smith, S., Yoshikawa, K. & Brown, J. Permafrost temperature records: Indicators of climate change. *EOS Trans. Am. Geophys. Union* **83**(50), 589–594. <https://doi.org/10.1029/2002EO000402> (2002).
24. Smith, M. W. & Riseborough, D. W. Permafrost monitoring and detection of climate change. *Permafrost Periglac. Process.* **7**(4), 301–309 (1996).
25. Dimri, A. P. et al. Climate change, cryosphere and impacts in the Indian Himalayan Region. *Curr. Sci.* **120**(5), 774–790 (2021).
26. Mukherji, A., Sinisalo, A., Nüsser, M., Garrard, R. & Eriksson, M. Contributions of the cryosphere to mountain communities in the Hindu Kush Himalaya: A review. *Reg. Environ. Change* **19**(5), 1311–1326. <https://doi.org/10.1007/s10113-019-01484-w> (2019).
27. Mahanta, K.K., Pradhan, I.P., Gupta, S.K., Singh, A., Gupta, P. & Shukla, D.P. Permafrost in Northern Hemisphere are shrinking at higher rate than in Southern Hemisphere. In *AGU Fall Meeting Abstracts* (Vol. 2022, pp. EP42A-47). Chicago, IL (2022). <http://ui.adsabs.harvard.edu/abs/2022AGUFMEP42A..47M>

28. Ding, Y. et al. Increasing cryospheric hazards in a warming climate. *Earth Sci. Rev.* **213**, 103500 (2021).
29. Käab, A. et al. Remote sensing of glacier-and permafrost-related hazards in high mountains: An overview. *Nat. Hazard.* **5**(4), 527–554 (2005).
30. Patton, A. I., Rathburn, S. L. & Capps, D. M. Landslide response to climate change in permafrost regions. *Geomorphology* **340**, 116–128 (2019).
31. Singh, A. et al. Comparing Landslide Susceptibility in Northwest and Northeast Himalaya: A Case Study of Kangra and Tamenglong Districts. in XXVIII General Assembly of the International Union of Geodesy and Geophysics (IUGG) (GFZ German Research Centre for Geosciences, Berlin, 2023). <https://doi.org/10.57757/IUGG23-4157>.
32. Singh, A., Dhiman, N., Niraj, K. C. & Shukla, D. P. “Ensembled transfer learning approach for error reduction in landslide susceptibility mapping of the data scarce region”. *Sci. Rep.* **14**, 29060 (2024).
33. Singh, A., Chhetri, N. K., Nitesh, Gupta, S. K. & Shukla, D. P. Strategies for sampling pseudo-absences of landslide locations for landslide susceptibility mapping in complex mountainous terrain of Northwest Himalaya. *Bull. Eng. Geol. Environ.* **82**, 321 (2023).
34. Singh, A. et al. Evaluating causative factors for landslide susceptibility along the Imphal-Jiribam railway corridor in the North-Eastern part of India using a GIS-based statistical approach. *Environ. Sci. Pollut. Res.* **31**, 53767–53784 (2024).
35. Singh, A. et al. Evaluating the effect of different sampling ratio on landslide susceptibility mapping of Kangra District. in vol. 2022 NH25D-0484 (2022).
36. Singh, A., Dhiman, N., K. C., N. & Shukla, D. P. Improving ML-based landslide susceptibility using ensemble method for sample selection: a case study of Kangra district in Himachal Pradesh, India. *Environ. Sci. Pollut. Res.* <https://doi.org/10.1007/s11356-024-34726-4>. (2024).
37. Jawak, S. D., Bidawe, T. G. & Luis, A. J. A review on applications of imaging synthetic aperture radar with a special focus on cryospheric studies. *Adv. Remote Sens.* <https://doi.org/10.4236/ars.2015.42014> (2015).
38. Teshebaeva, K. et al. Permafrost dynamics and degradation in polar Arctic from satellite radar observations, Yamal peninsula. *Front. Earth Sci.* **9**, 741556 (2021).
39. Zhang, Z., Wang, M., Wu, Z. & Liu, X. Permafrost deformation monitoring along the Qinghai-Tibet Plateau engineering corridor using InSAR observations with multi-sensor SAR datasets from 1997–2018. *Sensors* **19**(23), 5306 (2019).
40. Li, X. et al. Time-series InSAR monitoring of surface deformation in Yakutsk, a city located on continuous permafrost. *Earth Surf. Proc. Land.* **49**(2), 918–932. <https://doi.org/10.1002/esp.5736> (2024).
41. Zhang, Z. et al. A review of satellite synthetic aperture radar interferometry applications in permafrost regions: Current status, challenges, and trends. *IEEE Geosci. Remote Sens. Mag.* **10**(3), 93–114 (2022).
42. Singleton, A., Li, Z., Hoey, T. & Muller, J.-P. Evaluating sub-pixel offset techniques as an alternative to D-InSAR for monitoring episodic landslide movements in vegetated terrain. *Remote Sens. Environ.* **147**, 133–144 (2014).
43. Zhang, Z. et al. Monitoring and analysis of ground subsidence in Shanghai based on PS-InSAR and SBAS-InSAR technologies. *Sci. Rep.* **13**(1), 8031 (2023).
44. Fadhillah, M. F., Achmad, A. R. & Lee, C.-W. Improved combined scatterers interferometry with optimized point scatterers (ICOPS) for interferometric synthetic aperture radar (InSAR) time-series analysis. *IEEE Trans. Geosci. Remote Sens.* **60**, 1–14 (2021).
45. Mahanta, K. K., Singh, A., Gupta, S. K., Shukla, D. P. Tracking and Investigating Land Subsidence in Himalayan town using PSInSAR techniques: Lessons from Joshimath, XXVIII General Assembly of the International Union of Geodesy and Geophysics (IUGG) (2023).
46. Niraj, K. C., Gupta, S. K. & Shukla, D. P. Kotrupi landslide deformation study in non-urban area using DInSAR and MTInSAR techniques on Sentinel-1 SAR data. *Adv. Space Res.* **70**(12), 3878–3891. <https://doi.org/10.1016/j.asr.2021.11.042> (2022).
47. Tizzani, P. et al. Surface deformation of Long Valley caldera and Mono Basin, California, investigated with the SBAS-InSAR approach. *Remote Sens. Environ.* **108**(3), 277–289 (2007).
48. Zhou, P., Liu, W., Zhang, X. & Wang, J. Evaluating permafrost degradation in the Tuotuo river basin by MT-InSAR and LSTM methods. *Sensors* **23**(3), 1215 (2023).
49. Zwieback, S., Liu, L., Rouyet, L., Short, N. & Strozzi, T. Advances in InSAR analysis of permafrost terrain. *Permafrost Periglac. Process.* **35**(4), 544–556. <https://doi.org/10.1002/ppp.2248> (2024).
50. Hu, J., Li, Z., Ding, X., Zhu, J. & Sun, Q. Spatial-temporal surface deformation of Los Angeles over 2003–2007 from weighted least squares DInSAR. *Int. J. Appl. Earth Obs. Geoinf.* **21**, 484–492. <https://doi.org/10.1016/j.jag.2012.07.007> (2013).
51. Li, Z. et al. InSAR analysis of surface deformation over permafrost to estimate active layer thickness based on one-dimensional heat transfer model of soils. *Sci. Rep.* **5**(1), 15542. <https://doi.org/10.1038/srep15542> (2015).
52. Lu, P., Han, J., Hao, T., Li, R. & Qiao, G. Seasonal deformation of permafrost in Wudaoliang basin in Qinghai-Tibet Plateau revealed by StaMPS-InSAR. *Mar. Geodesy* **43**(3), 248–268. <https://doi.org/10.1080/01490419.2019.1698480> (2020).
53. Strozzi, T. et al. Sentinel-1 SAR Interferometry for surface deformation monitoring in low-land permafrost areas. *Remote Sens.* <https://doi.org/10.3390/rs10091360> (2018).
54. Wang, C. et al. Active layer thickness retrieval of Qinghai-Tibet permafrost using the TerraSAR-X InSAR technique. *IEEE J. Select. Top. Appl. Earth Obs. Remote Sens.* **11**(11), 4403–4413. <https://doi.org/10.1109/JSTARS.2018.2873219> (2018).
55. Zhao, R., Li, Z., Feng, G., Wang, Q. & Hu, J. Monitoring surface deformation over permafrost with an improved SBAS-InSAR algorithm: With emphasis on climatic factors modeling. *Remote Sens. Environ.* **184**, 276–287. <https://doi.org/10.1016/j.rse.2016.07.019> (2016).
56. Krishnanand, K., & Raman, V. A. V. *Geographical analysis of geotourism based seasonal economy in Lahaul and Spiti, Himachal Pradesh (India)*. <https://doi.org/10.5555/20193212744> (2019).
57. DéZes, P. J., Vannay, J., Steck, A., Bussy, F. & Cosca, M. Synorogenic extension: Quantitative constraints on the age and displacement of the Zaskar shear zone (northwest Himalaya). *GSA Bull. GeoScienceWorld* [https://doi.org/10.1130/0016-7606\(1999\)111](https://doi.org/10.1130/0016-7606(1999)111) (1999).
58. Srikantia, S. V. & Bhargava, O. N. The Tandi Group of Lahaul-its geology and relationship with the Central Himalayan Gneiss. *J. Geol. Soc. India* **20**(11), 531–539 (1979).
59. Stübner, K. et al. Monazite geochronology unravels the timing of crustal thickening in NW Himalaya. *Lithos* **210–211**, 111–128. <https://doi.org/10.1016/j.lithos.2014.09.024> (2014).
60. Eppard, J.-L., Steck, A., Vannay, J.-C. & Hunziker, J. Tertiary Himalayan structures and metamorphism in the Kulu Valley (Mandi-Khoksar transect of the Western Himalaya)—Shikar-Beh-Nappe and Crystalline Nappe. *Schweiz. Mineral. Petrogr. Mitt.* **75**, 59–84 (1995).
61. Thöni, M., Miller, C., Hager, C., Grasmann, B. & Horsching, M. New geochronological constraints on the thermal and exhumation history of the Lesser and Higher Himalayan Crystalline Units in the Kullu-Kinnaur area of Himachal Pradesh (India). *J. Asian Earth Sci.* **52**, 98–116. <https://doi.org/10.1016/j.jseas.2012.02.015> (2012).
62. Bekaert, D. P., Handwerker, A. L., Agram, P. & Kirschbaum, D. B. InSAR-based detection method for mapping and monitoring slow-moving landslides in remote regions with steep and mountainous terrain: An application to Nepal. *Remote Sens. Environ.* **249**, 111983. <https://doi.org/10.1016/j.rse.2020.111983> (2020).
63. Hersbach, H. et al. The ERA5 global reanalysis. *Q. J. R. Meteorol. Soc.* **146**(730), 1999–2049. <https://doi.org/10.1002/qj.3803> (2020).

64. Hrysiewicz, A., Wang, X. & Holohan, E. P. EZ-InSAR: An easy-to-use open-source toolbox for mapping ground surface deformation using satellite interferometric synthetic aperture radar. *Earth Sci. Inf.* **16**(2), 1929–1945. <https://doi.org/10.1007/s12145-023-00973-1> (2023).
65. Rosen, P. A., Gurrola, E., Sacco, G. F., & Zebker, H. The InSAR scientific computing environment. *EUSAR 2012; 9th European Conference on Synthetic Aperture Radar*, 730–733. <https://ieeexplore.ieee.org/abstract/document/6217174>. (2012).
66. Yunjun, Z., Fattahi, H. & Amelung, F. Small baseline InSAR time series analysis: Unwrapping error correction and noise reduction. *Comput. Geosci.* **133**, 104331. <https://doi.org/10.1016/j.cageo.2019.104331> (2019).
67. Xu, X. & Sandwell, D. T. Toward absolute phase change recovery with InSAR: Correcting for earth tides and phase unwrapping ambiguities. *IEEE Trans. Geosci. Remote Sens.* **58**(1), 726–733. <https://doi.org/10.1109/TGRS.2019.2940207> (2020).
68. Pepe, A. & Lanari, R. On the extension of the minimum cost flow algorithm for phase unwrapping of multitemporal differential SAR interferograms. *IEEE Trans. Geosci. Remote Sens.* **44**(9), 2374–2383. <https://doi.org/10.1109/TGRS.2006.873207> (2006).
69. Jolivet, R. et al. Improving InSAR geodesy using global atmospheric models. *J. Geophys. Res. Solid Earth* **119**(3), 2324–2341. <https://doi.org/10.1002/2013JB010588> (2014).
70. Jolivet, R., Grandin, R., Lasserre, C., Doin, M.-P. & Peltzer, G. Systematic InSAR tropospheric phase delay corrections from global meteorological reanalysis data. *Geophys. Res. Lett.* <https://doi.org/10.1029/2011GL048757> (2011).
71. Fattahi, H. & Amelung, F. DEM error correction in InSAR time series. *IEEE Trans. Geosci. Remote Sens.* **51**(7), 4249–4259. <https://doi.org/10.1109/TGRS.2012.2227761> (2013).
72. Hetland, E. A. et al. Multiscale InSAR Time Series (MINTS) analysis of surface deformation. *J. Geophys. Res. Solid Earth* <https://doi.org/10.1029/2011JB008731> (2012).
73. Lohman, R. B. & Simons, M. Some thoughts on the use of InSAR data to constrain models of surface deformation: Noise structure and data downsampling. *Geochem. Geophys. Geosyst.* <https://doi.org/10.1029/2004GC000841> (2005).
74. Sudhaus, H. & Sigurjón, J. Improved source modelling through combined use of InSAR and GPS under consideration of correlated data errors: Application to the June 2000 Kleifarvatn earthquake, Iceland. *Geophys. J. Int.* **176**(2), 389–404. <https://doi.org/10.1111/j.1365-246X.2008.03989.x> (2009).
75. Hersbach, H., Bell, B., Berrisford, P., Biavati, G., Horányi, A., Sabater, J. M., Nicolas, J., Peubey, C., Radu, R., & Rozum, I. *ERA5 Hourly Data on Pressure Levels from 1940 to Present: Tech. Rep.* (2023).
76. Ahmed, S. M. Assessment of irrigation system sustainability using the Theil-Sen estimator of slope of time series. *Sustain. Sci.* **9**(3), 293–302. <https://doi.org/10.1007/s11625-013-0237-1> (2014).
77. Mudelsee, M. Trend analysis of climate time series: A review of methods. *Earth Sci. Rev.* **190**, 310–322. <https://doi.org/10.1016/j.earscirev.2018.12.005> (2019).
78. Pradhan, I. P., Mahanta, K. K., Liou, Y.-A., Chauhan, A. & Shukla, D. P. Machine learning based high-resolution air temperature modelling from landsat-8, MODIS, and in-situ measurements with ERA-5 inter-comparison in the data sparse regions of Himachal Pradesh. *Bull. Atmos. Sci. Technol.* **5**(1), 22. <https://doi.org/10.1007/s42865-024-00085-8> (2024).
79. Yue, S. & Wang, C. Y. Applicability of prewhitening to eliminate the influence of serial correlation on the Mann-Kendall test. *Water Resour. Res.* <https://doi.org/10.1029/2001WR000861> (2002).
80. Pradhan, I. P. & Shukla, D. P. Assessment of the Accuracy of Satellite-Derived Land Surface Temperature with IMD In-Situ Air Temperature: A Case Study for Kullu Region, Himachal Pradesh, India. in *IGARSS 2022 - 2022 IEEE International Geoscience and Remote Sensing Symposium* 40–43 (2022). <https://doi.org/10.1109/IGARSS46834.2022.9884649>
81. Liu, L. & Larson, K. M. Decadal changes of surface elevation over permafrost area estimated using reflected GPS signals. *Cryosphere* **12**(2), 477–489. <https://doi.org/10.5194/tc-12-477-2018> (2018).
82. Shugar, D. H. et al. A massive rock and ice avalanche caused the 2021 disaster at Chamoli, Indian Himalaya. *Science* **373**(6552), 300–306. <https://doi.org/10.1126/science.abh4455> (2021).
83. Banerjee, S. Deformation trail tracking in S-tectonites of the Darjeeling-Sikkim Himalaya: The kink band perspective. *J. Asian Earth Sci.* **256**, 105827. <https://doi.org/10.1016/j.jseas.2023.105827> (2023).
84. Rawat, A., Banerjee, S., Sundriyal, Y. & Rana, V. An integrated assessment of the geomorphic evolution of the Garhwal synform: Implications for the relative tectonic activity in the southern part of the Garhwal Himalaya. *J. Earth Syst. Sci.* **131**(1), 56. <https://doi.org/10.1007/s12040-021-01794-w> (2022).
85. Singh, S., Raju, A. & Banerjee, S. Detecting slow-moving landslides in parts of Darjeeling-Sikkim Himalaya, NE India: Quantitative constraints from PSInSAR and its relation to the structural discontinuities. *Landslides* **19**(10), 2347–2365. <https://doi.org/10.1007/s10346-022-01900-z> (2022).
86. Singh, A., Niranjannaik, M., Kumar, S. & Gaurav, K. Comparison of different dielectric models to estimate penetration depth of L- and S-Band SAR signals into the ground surface. *Geographies* <https://doi.org/10.3390/geographies2040045> (2022).
87. Jade, S. et al. India plate angular velocity and contemporary deformation rates from continuous GPS measurements from 1996 to 2015. *Sci. Rep.* **7**(1), 11439. <https://doi.org/10.1038/s41598-017-11697-w> (2017).
88. Jade, S. et al. Crustal deformation rates in Kashmir valley and adjoining regions from continuous GPS measurements from 2008 to 2019. *Sci. Rep.* **10**(1), 17927. <https://doi.org/10.1038/s41598-020-74776-5> (2020).
89. Garzanti, E., Baud, A. & Mascle, G. Sedimentary record of the northward flight of India and its collision with Eurasia (Ladakh Himalaya, India). *Geodyn. Acta* **1**, 87–102 (1987).
90. Searle, M. P. et al. The closing of Tethys and the tectonics of the Himalayas. *Geol. Soc. Am. Bull.* **98**, 678–701 (1987).
91. Walker, J. et al. Metamorphism, melting, and extension: age constraints from the High Himalayan Slab of southeast Zaskar and northwest Lahul. *J. Geol.* **107**, 473–495 (1999).
92. Steck, A., Epard, J.-L. & Robyr, M. The NE-directed Shikar Beh Nappe: a major structure of the Higher Himalaya. *Eclogae Geol. Helv.* **92**, 239–250 (1999).
93. Vannay, J.-C. & Steck, A. Tectonic evolution of the High Himalaya in Upper Lahul (NW Himalaya India). *Tectonics* **14**, 253–263 (1995).
94. Epard, J. & Steck, A. The Eastern prolongation of the Zaskar Shear Zone (Western Himalaya). *Eclogae Geol. Helv.* **97**(2), 193–212. <https://doi.org/10.1007/s00015-004-1116-7> (2004).
95. Deshmukh, G. G. et al. South Tibetan Detachment System (STDS), NW Himalaya: A possible Cambro-Ordovician tectonic terrane boundary, and its Cenozoic remobilization. *Gondwana Res.* **136**, 142–168. <https://doi.org/10.1016/j.gr.2024.08.008> (2024).
96. Webb, A. U-Pb zircon geochronology of major lithologic units in the eastern Himalaya: Implications for the origin and assembly of Himalayan rocks. *Geol. Soc. Am. Bull.* **125**(3–4), 499–522. <https://doi.org/10.1130/b30626.1> (2012).
97. Yin, A. & Harrison, T. M. Geologic evolution of the Himalayan-Tibetan Orogen. *Annu. Rev. Earth Planet Sci.* **28**, 211–280 (2000).
98. Schuur, E. a. G. et al. Climate change and the permafrost carbon feedback. *Nature* **520**, 171–179 (2015).
99. Hjort, J. et al. Degrading permafrost puts Arctic infrastructure at risk by mid-century. *Nat. Commun.* **9**, 5147 (2018).
100. Kaushik, S., Dharpure, J. K., Joshi, P. K., Ramanathan, A. & Singh, T. Climate change drives glacier retreat in Bhaga basin located in Himachal Pradesh, India. *Geocarto Int.* **35**(11), 1179–1198. <https://doi.org/10.1080/10106049.2018.1557260> (2020).
101. Prakash, S., Sharma, M. C., Deswal, S. & Kumar, P. Cryospheric changes and livelihood vulnerability in Lahaul Region of North-Western Himalaya, India. *Sustain. Water Resour. Manag.* **10**(6), 194. <https://doi.org/10.1007/s40899-024-01170-8> (2024).
102. Bernier, M. & Fortin, J.-P. The potential of times series of C-Band SAR data to monitor dry and shallow snow cover. *IEEE Trans. Geosci. Remote Sens.* **36**(1), 226–243. <https://doi.org/10.1109/36.655332> (1998).

Acknowledgements

The authors are grateful to IIT Mandi in Kamand, Himachal Pradesh, India, for providing this opportunity and technical tools to conduct this research. This work was supported by the Prime Minister's Research Fellowship (PMRF) award being provided to the first author KKM (Application No. 2603558). Additionally, we would like to thank the contributor of EZ-InSAR and MintPy for providing their open-source software for the analysis. Also, the authors would like to acknowledge the ESA for providing the Sentinel 1 imagery to carry out this work.

Author contributions

Kirti Kumar Mahanta: data curation, formal analysis, investigation, validation, visualization, roles/writing—original draft; Ipshita Priyadarsini Pradhan: data curation, formal analysis, investigation, roles/writing—original draft; Nitesh Dhiman: data curation, formal analysis, investigation; Ankit Singh: data curation, formal analysis, investigation; Dericks Praise Shukla: conceptualization, formal analysis, investigation, methodology, resources, software, supervision, validation, writing—review and editing.

Declarations

Competing interests

The authors declare no competing interests.

Consent for publication

All authors give their consent to publish this work in whole.

Additional information

Supplementary Information The online version contains supplementary material available at <https://doi.org/10.1038/s41598-025-03921-9>.

Correspondence and requests for materials should be addressed to D.P.S.

Reprints and permissions information is available at www.nature.com/reprints.

Publisher's note Springer Nature remains neutral with regard to jurisdictional claims in published maps and institutional affiliations.

Open Access This article is licensed under a Creative Commons Attribution-NonCommercial-NoDerivatives 4.0 International License, which permits any non-commercial use, sharing, distribution and reproduction in any medium or format, as long as you give appropriate credit to the original author(s) and the source, provide a link to the Creative Commons licence, and indicate if you modified the licensed material. You do not have permission under this licence to share adapted material derived from this article or parts of it. The images or other third party material in this article are included in the article's Creative Commons licence, unless indicated otherwise in a credit line to the material. If material is not included in the article's Creative Commons licence and your intended use is not permitted by statutory regulation or exceeds the permitted use, you will need to obtain permission directly from the copyright holder. To view a copy of this licence, visit <http://creativecommons.org/licenses/by-nc-nd/4.0/>.

© The Author(s) 2025